Supplemental Information for

Mn 2p and O 1s X-ray absorption spectroscopy of manganese oxides

Haytham Eraky[1], James J. Dynes[2] and Adam P. Hitchcock[1*]

[1]Dept of Chemistry & Chemical Biology, McMaster University, Hamilton, ON, Canada L8S4M1

[2]Canadian Light Source, Saskatoon, Saskatchewan, Canada S7N2V3

Contents

SI.1 Origin of Mn 2p and O 1s spectral features of MnO_x species

SI.2 X-ray diffraction powder patterns

SI.3 Incident flux normalization in STXM and TEY

SI.4 Comparison of MnO_2 spectra measured in TEY, TFY and PFY modes

SI.5 Sensitivity of the Mn 2p STXM spectrum of MnO to absorption saturation

SI.6 Conversion of measured OD spectra to quantitative OD1 spectra

SI.7 Spectral energy calibration using gas phase spectroscopy

SI.8 Exploration of difference in SM and SGM energy scales

SI.9 CLS-SM energy scale stability over a 5-day period

SI.10 Comparison of our results for MnO_2 to those of Gilbert [S4] and Toner [S17]

SI.11 O 1s spectra of compounds with different sulfur-oxygen bond length

SI.12 Comparison of the O 1s spectra of α-MnO_2 and β-MnO_2

SI.13 Comparison of analyses using Mn 2p, O 1s and (O 1s & Mn 2p) stacks

SI.14 Example of linear combination fitting (LCF) of a mixed oxide spectrum

SI.1 Origin of Mn 2p and O 1s spectral features of MnO_x species

The 2p absorption spectra of 3d transition metals (manganese in this case) are dominated by dipole allowed 2p → 3d transitions which probe the empty valence levels of the absorbing atom which, in turn, depend on the geometric and electronic structure of the compound [S1,S2]. As the Mn oxidation state increases, the binding energy of the Mn 2p core level increases, leading to systematic shifts of the X-ray absorption spectral features to higher energy. At the O 1s edge it is the presence of empty electronic states with combined O 2p and Mn 3d character that leads to characteristic O 1s → Mn 3d features in the low energy region (528 – 534 eV), thus enabling differentiation of the Mn oxidation states at the O 1s edge [S3].

The sharp features in the manganese 2p spectra arise from transitions from the ($2p^6..3d^n$) ground state to ($2p^5..d^{n+1}$) excited states in which the dominant electronic configuration features a Mn 2p core hole and an excited electron in a specific unoccupied orbital / band. There are four major interactions which determine the fine details of the Mn 2p NEXAFS spectra. The strongest interaction is **spin-orbit splitting**, which gives rise to two distinct bands separated by ~11 eV. The spin-orbit splitting arises from the strong interaction of the net l=1 orbital angular momentum of the $2p^5$ core level with the unpaired spin [S4-S6].

The next strongest interaction is the **crystal field splitting**, resulting from electrostatic interaction of the positively charged Mn ion and the field generated by the array of surrounding, negatively charged O ions. The energy difference between the t_{2g} and e_g orbitals defines the crystal field strength (Δo or 10 Dq) [S7]. The magnitude of the crystal-field splitting depends on the Mn oxidation state and the nature of the coordinating anions, since the energies of the 3d-orbitals are influenced by ligand symmetries as well as strength of the Mn – O interaction [S8]. The Mn 3d and O 2p atomic orbitals interact to form both σ-bonding and π-bonding orbitals [S8,S9]. The σ-bonds can be described in terms of lobes of the Mn d(x^2 - y^2) and d($3z^2$ – r^2) orbitals being aligned with lobes of the O 2p-orbitals.The π –bonds result from overlap of the Mn d(xy), d(yz) and d(xz) orbitals with O 2p-orbitals oriented perpendicular to the metal - ligand vector [S9].

Next, depending on the strength of the crystal field splitting relative to the **pairing energy** (stabilization of an electronic system by forming electron pairs), the electrons can be arranged in either high-spin or low-spin arrangements, which affects the occupancy of the unoccupied Mn 3d levels. The $3d^4$ configuration of Mn(II) and $3d^5$ configuration of Mn(III) can exist in either high-spin or low-spin arrangements. Low-spin Mn(II) compounds are rarely found in nature due to the large crystal field splitting required for a low-spin ground state. On the other hand, Mn(III) normally exists in the low-spin state, but can be stabilized in a high-spin state due to Jahn-Teller distortion of its coordination environment. The octahedrally coordinated Mn(IV) with a $3d^3$ electron configuration exists only in the high-spin configuration.

Finally, the spin-orbit interaction among partially filled Mn 3d levels gives rise to **atomic multiplet splittings** [S10]. Manganese oxides can exhibit multiplet splittings, depending on the oxidation state. $KMnO_4$ should not exhibit multiplet splittings since the dominant low-spin configuration does not have unpaired electrons. However, the partial covalency from O 2p – Mn 3d mixing in $KMnO_4$ introduces a partially occupied d-orbital character, leading to multiplet splitting [S11]. The Mn 2p spectra of MnO, Mn_2O_3 and MnO_2 can have multiplet splitting features since there are unpaired 3d electrons in all of these systems.

The O 1s pre-edge reflects the O 2p component of the **(Mn 3d, O 2p) hybridized empty states** in which the overlap of the empty Mn 3d and O 2p states depends on the orbital symmetry and the Mn-O bond length.

SI.2 X-ray diffraction powder patterns

Figure S.1 shows the X-ray diffraction patterns of the MnO, $MnSO_4$, Mn_3O_4, Mn_2O_3, α-MnO_2 and $KMnO_4$ samples studied. Comparison of the observed diffraction patterns with those in the Joint Committee on Powder Diffraction Standards (JCPDS) database indicates the samples are pure phases for all measured species: manganosite MnO (JCPDS PDF 04-008-0277), szmikite

$MnSO_4.(H_2O)$ (JCPDS PDF 04-008-9679), bixbyite Mn_2O_3 (PDF 00-041-1442), hausmannite Mn_3O_4 (JCPDS PDF 001-1127), α-MnO_2 (JCPDS PDF 00-044-0141), β-MnO_2 (JCPDS PDF 00-024-0735) and $KMnO_4$ (JCPDS PDF 04-008-2764).

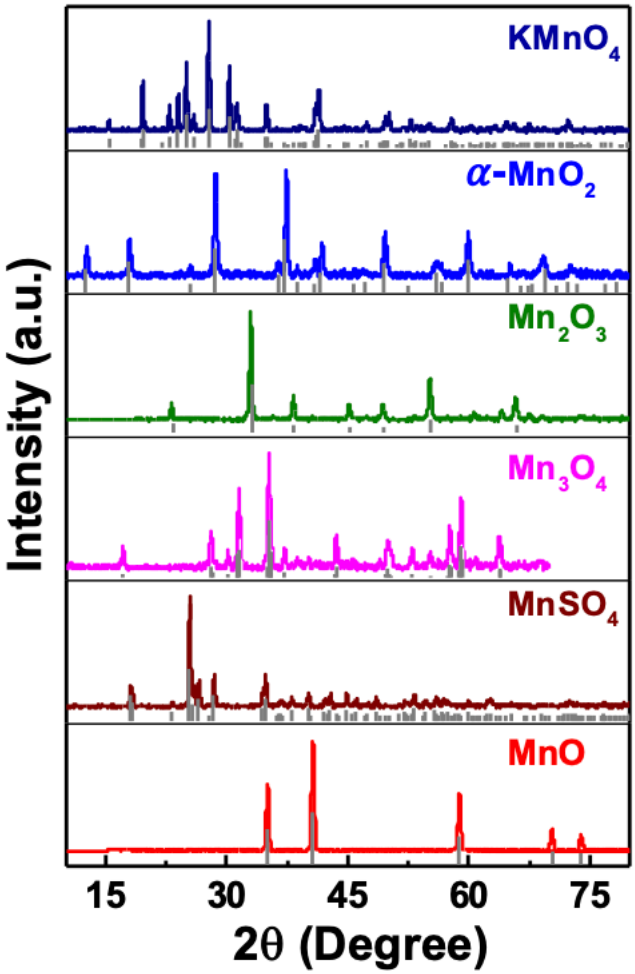

Figure S.1 **X-ray diffraction patterns** of MnO, $MnSO_4$, Mn_3O_4, Mn_2O_3, α-MnO_2, and $KMnO_4$. The grey lines are the JCPDS patterns for each compound.

SI.3 Incident flux normalization in STXM and TEY

Figure S.2A presents the measured sample current and gold-mesh Io signals recorded for the O 1s TEY spectrum of α-MnO_2. While there is observable O 1s spectral features in the Io signal, it does not appreciably affect the normalized O 1s spectral shape (**Fig. S.2B**). **Figure S.2C** presents the measured O 1s transmission signal from the MnO_2 sample in the region indicated in

the insert image, and the Io signal from an adjacent region off the sample. Again, there are strong O 1s spectral features in the Io. However, when one applies the Beers-Law conversion to optical density, *OD = -ln (I/Io)*, the correct spectral shape is obtained (**Fig. S.2D**).

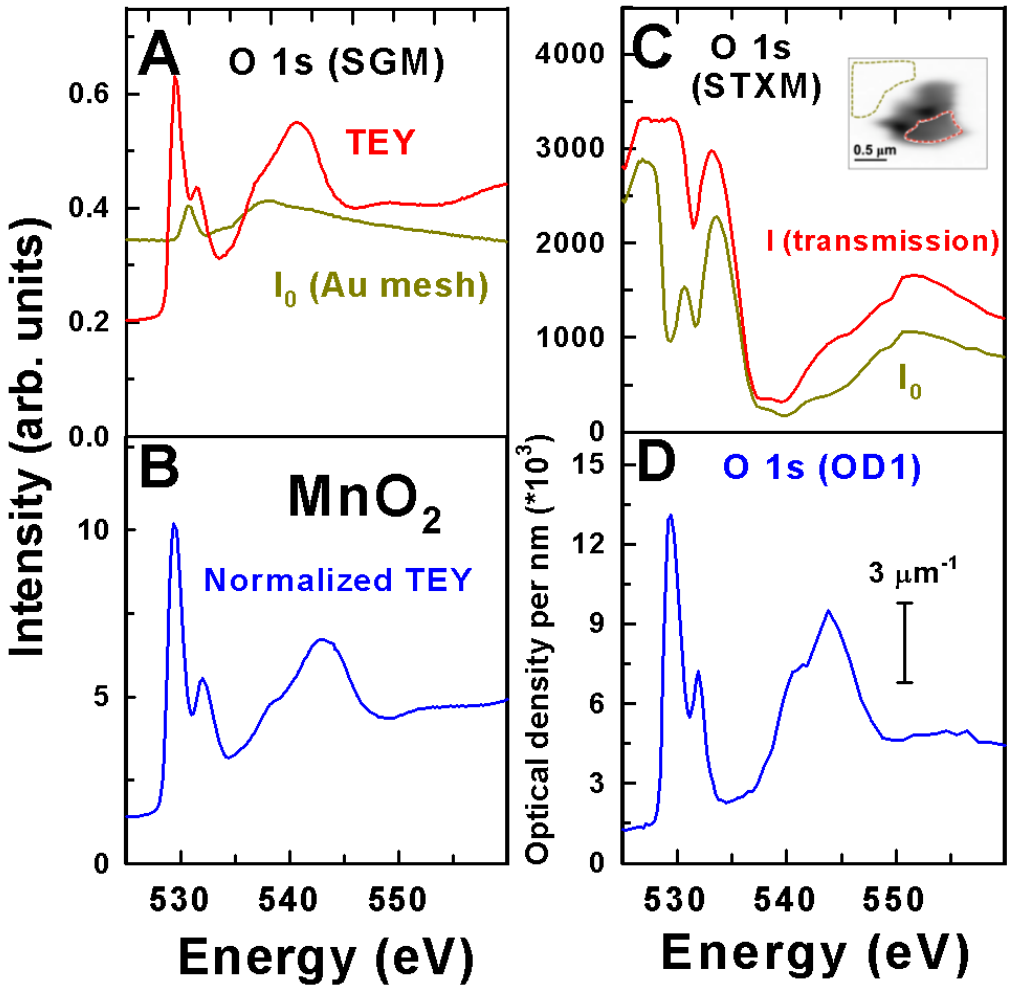

Figure S.2 Effect of structured Io signals on TEY and STXM O 1s spectra of α-MnO_2. (A) Plot of O 1s TEY (sample current) spectra of α-MnO_2 and the signal from the upstream Au mesh. (**B**) TEY spectrum divided by the Io mesh signal. (**C**) Plot of the O 1s transmission signal for α-MnO_2 and the Io transmission signal recorded from an adjacent off-sample location (see red (I) and green (Io) outlined areas of the inserted image). (**D**) O 1s absorption spectrum of α-MnO_2 derived by Beer's Law conversion [OD = -ln(I/Io)] of the I and Io transmission signals in **C**.

SI.4 Comparison of MnO_2 spectra measured in TEY, TFY and PFY modes

Figure S.3 compares the Mn 2p absorption spectra measured at the CLS spherical grating monochromator (SGM) beamline using the total electron yield (TEY), total fluorescence yield (TFY), and partial fluorescence yield (PFY, Mn Lα) modes. Relative to the Mn $2p_{1/2}$ signal, the Mn $2p_{3/2}$ signal in the TFY and PFY modes is significantly reduced as compared to TEY spectrum. The reduction of the Mn $2p_{3/2}$ intensity is caused by absorption saturation due to a too-thick sample.

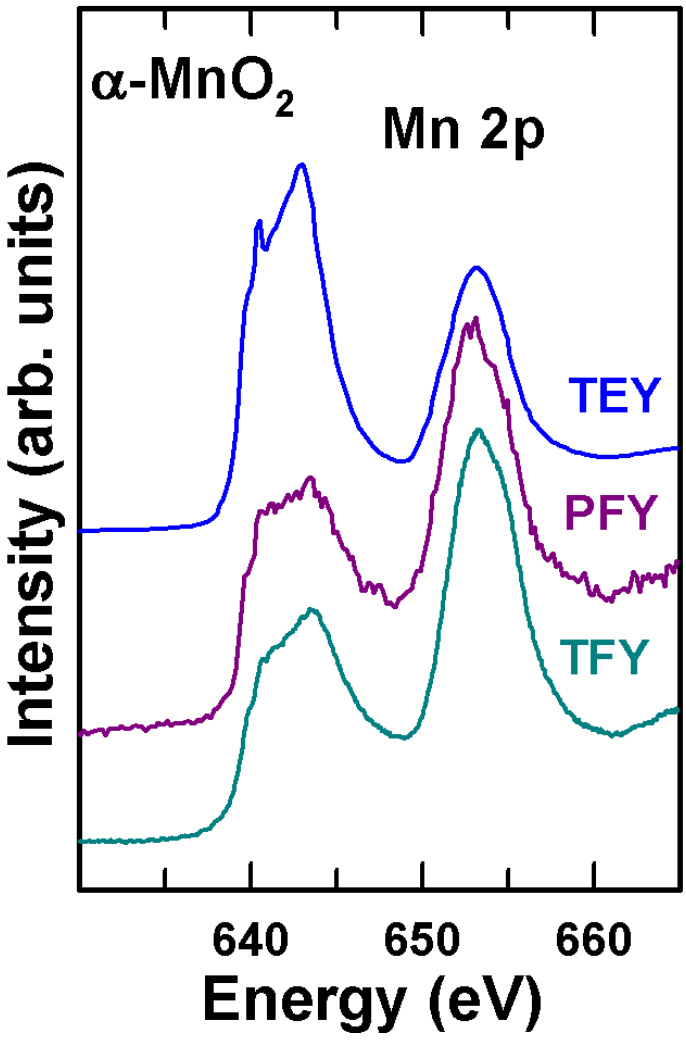

Figure S.3 Comparison of Mn 2p spectra of α-MnO_2 measured with the SGM beamline in total electron yield (TEY), total fluorescence yield (TFY) and partial fluorescence yield (PFY) modes.

SI.5 Sensitivity of the Mn 2p STXM spectrum of MnO to absorption saturation

Figure S.4 prevents evidence of the facile distortion by absorption saturation of the strong Mn 2p peak of MnO. In addition, it explores the ability of STXM to both detect and measure meaningful X-ray absorption spectra from extremely small amounts of material.

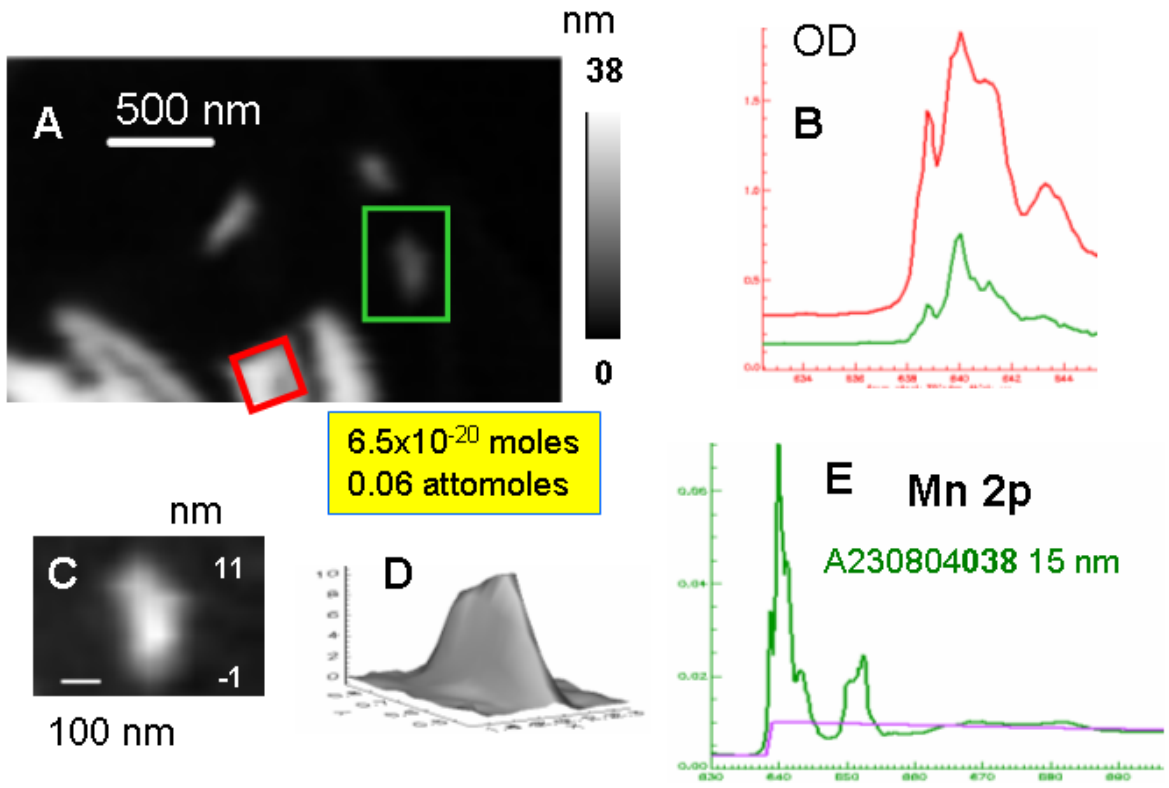

Figure S.4 Demonstration of sensitivity to absorption saturation of the Mn 2p spectrum of MnO. **(A)** Quantitative map of (absorption unsaturated) MnO from a stack measured on an 80 nm thick microtomed sample. **(B)** Mn 2p spectra of the red and green areas highlighted in A. **(C)** quantitative thickness map of the small particle in the green box. **(D)** 3D display of the particle. (E) derived Mn 2p spectrum, which is estimated to have been measured on 0.06 attomoles, or 40,000 repeat units of MnO.

SI.6 Conversion of measured OD spectra to quantitative OD1 spectra

In order to generate quantitative thickness maps of individual chemical species, we use optical density per nm thickness at standard densities – so-called OD1 intensity scales. **Figure S.5** shows a step-by-step procedure to generate optical density elemental response curves (**S.5C**) for a given chemical species, in this case MnO, from the elemental mass absorption coefficients (**S.5A, B**) which can be downloaded from the Centre for X-ray Optics website (https://henke.lbl.gov/optical_constants/) [S12]. Once the elemental response for the composition and density of the material is generated (**S.5D**), which can done in aXis2000 using the menu item, *Utilities~Calculate X-ray parameters (sf)*), the ratio of a measured OD spectrum of the material to that of the elemental OD1 curve is calculated. A scale factor (**S.5E**), which is the average of the ratios in the pre-edge (below start of first spectral feature) and the far-continuum (>30 eV above the first spectral feature), is used to convert the measured OD spectrum to the OD1 spectrum of the material (**S.5F**).

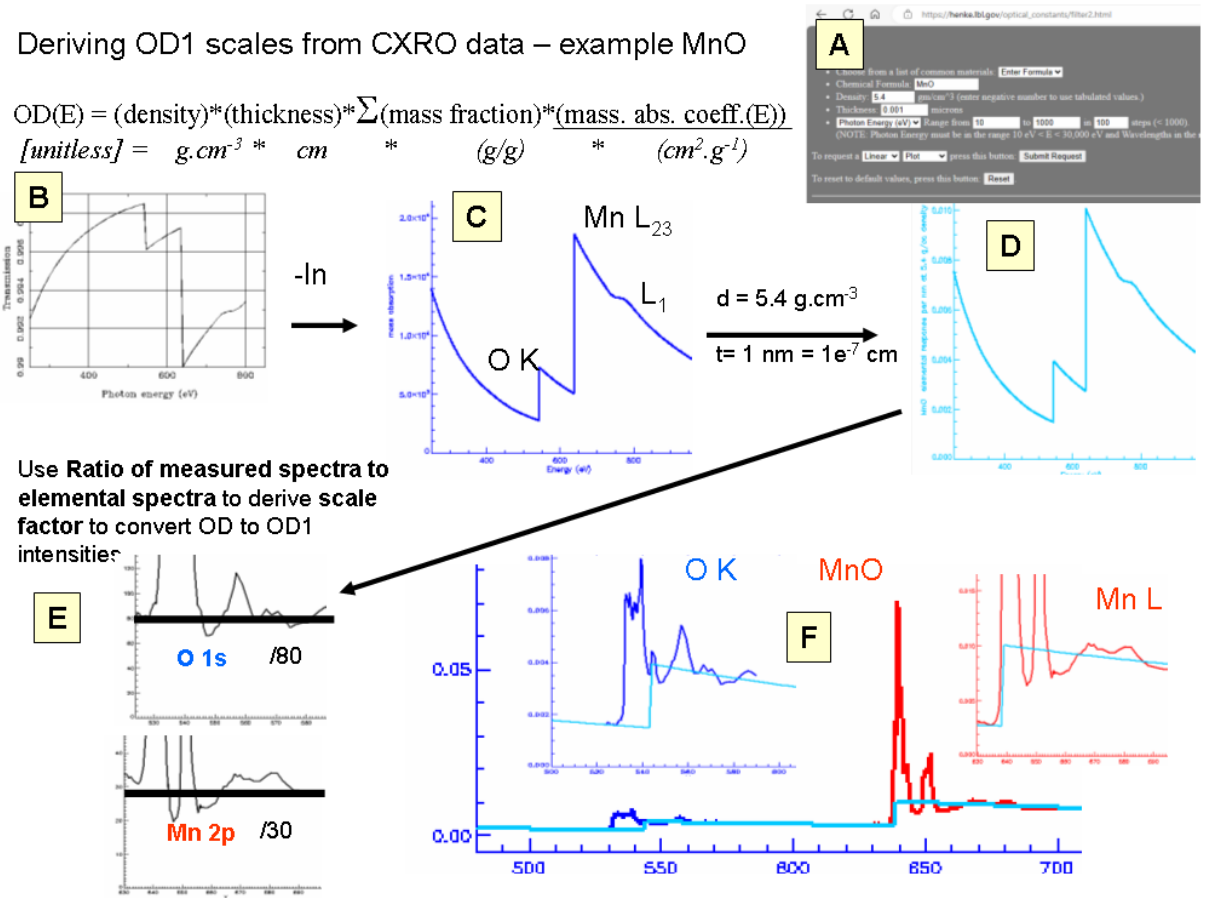

Figure S.5 Derivation of OD1 elemental response for MnO from the elemental mass absorption cross sections for Mn and O reported in the CXRO website (https://henke.lbl.gov/optical_constants/). Note that the mass absorption cross sections for the metal L_{23} spectra of the 3d transition elements reported in the CXRO database indicate only one continuum for the combined signal of the L_3 and L_2 components. While in principle there should be two separate step edges in the Mn L_{23} portion of the spectrum, since the scale factor used to derive the OD1 scale is based on matching below 636 eV and above 666 eV (Fig. **S.5E**), the shape of the spectrum between these energies is not relevant.

Figure S.6A plots the STXM-derived, O 1s OD spectrum of α-MnO_2. The step curve is the OD1 elemental response function of MnO_2 (d = 5.08 g/cm^3) multiplied by 110, which is the thickness in nm of the sample. **Figure S.6B** plots the Mn 2p OD1 spectrum of α-MnO_2 in comparison with the elemental OD1 step curve. **Figure S.6C** plots the STXM-derived, Mn 2p OD spectrum of α-MnO_2. The step curve is the OD1 elemental response function multiplied by 35. **Figure S.6D** plots the Mn 2p OD1 spectrum of α-MnO_2 in comparison with the elemental OD1 step curve.

The OD1 elemental response is the spectrum for 1 nm of α-MnO_2 from the elemental cross-sections of Mn and O [S12], and the density of α-MnO_2 (5.08 g/cm^{-3} [S13]).

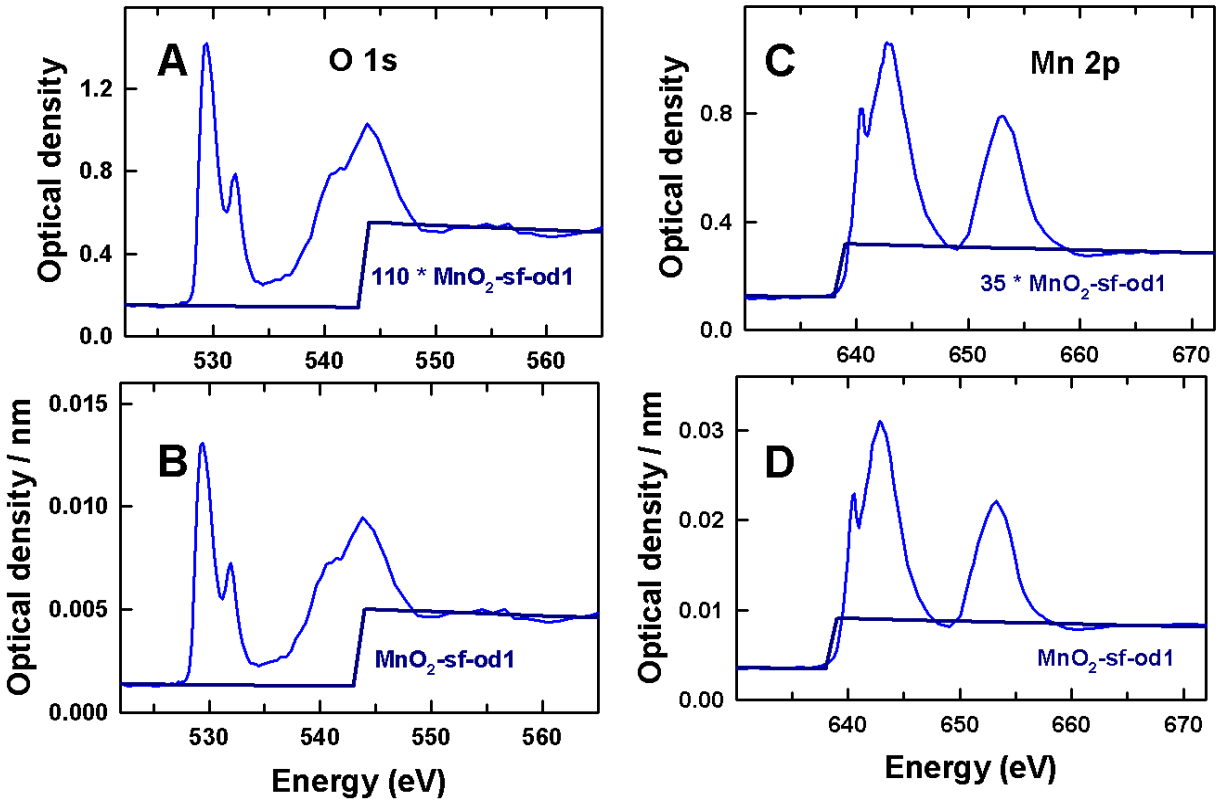

Figure S.6 Generation of absolute intensity reference spectra. (A) plot of the measured O 1s STXM spectrum of α-MnO_2 compared to that of 110 nm of the elemental response. (**B)** plot of the O 1s OD1 spectrum (OD / 110) compared to the elemental OD1 spectrum of α-MnO_2. (**C)** Plot of the measured Mn 2p STXM spectrum of α-MnO_2 compared to that of 35 nm of the elemental response. A thinner region was measured to avoid absorption saturation. (**D)** plot of the Mn 2p OD1 spectrum (OD / 35) compared to the elemental OD1 spectrum of α-MnO_2.

SI.7 Spectral energy calibration using gas phase spectroscopy

Figure S.7A presents STXM measurement of SF_6 gas in comparison with the literature F 1s spectrum of SF_6 [S14] **Figure S.7B** and **S.7C** present SGM (TEY mode) measurements of SF_6 gas and CO_2 gas measured in both fast scan and step scan modes before and after measuring the MnOx samples. The dotted lines indicate the position of the F 1s → a_{1g} peak of SF_6 (688.27 eV

[S14]) and O 1s → 3s peak of CO_2 (538.9 eV [S15]) used for calibration. The similarity of the positions of these peaks in both step and fast scans spectra confirm correct generation of the energy scale in the fast scan mode, as well as the excellent stability of the SGM energy scale.

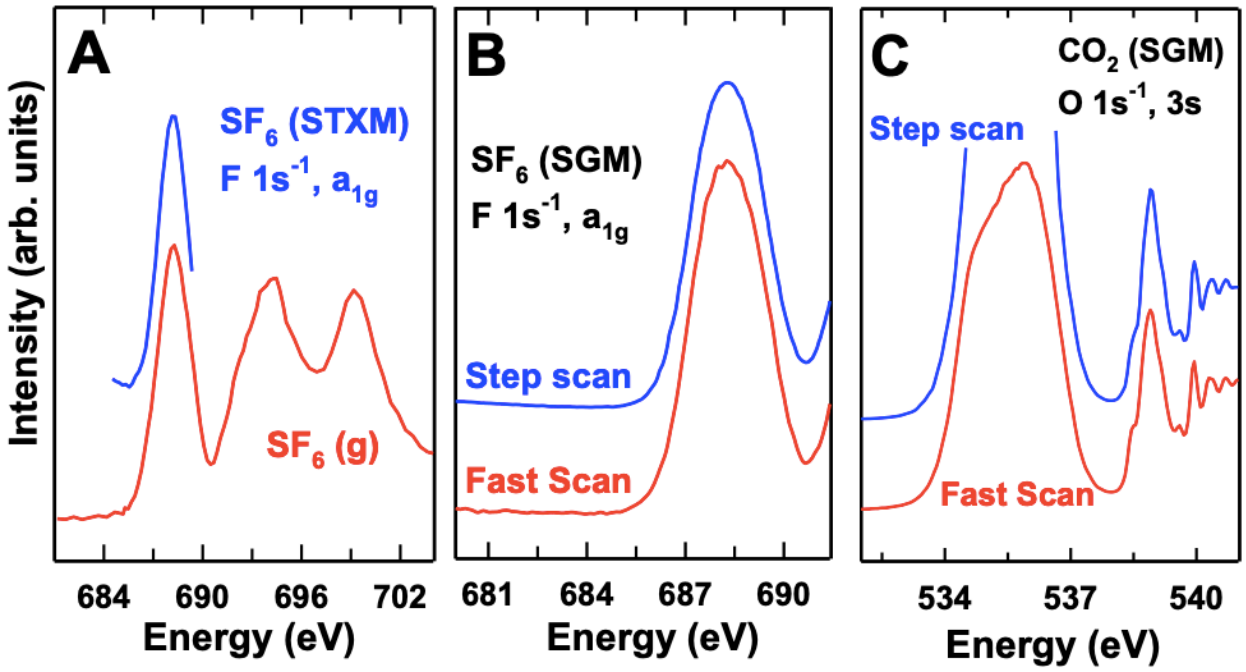

Fig. S.7 Energy calibration using gas phase spectroscopy. (A) F 1s spectra of SF_6 gas measured by STXM in comparison with the literature F 1s spectrum of SF_6 [S14]**. (B)** F 1s spectra of SF_6 gas measured with the step scan and fast scan (continuous non-linear slewing of the monochromator). **(C)** O 1s spectra of CO_2 gas measured with the step scan and fast scan (continuous non-linear slewing of the monochromator). The difference of the observed position and the known positions (SF_6 688.27(5) eV [S14]; O 1s, 3s peak, 538.9(1) eV [S15]) was used to calibrate the energy scales of the Mn 2p and O 1s spectra, respectively.

SI.8 Exploration of differences in SM and SGM energy scales

When comparing measurements at the Cu 2p, Ni 2p and Mn 2p edges made using TEY detection on the CLS-SGM beamline with those made on the CLS-SM beamline, we found differences in the spin-orbit splitting, which could be indicative of non-linear energy scales in one of the two beamline control systems, or possibly both. Since we rely on the linearity of the energy scale for accurate calibration of the Mn 2p energy scale using the F 1s → a_{1g} transition in SF_6 (g), it is important to understand how non-linear energy scales would affect the accuracy of our results. **Figure S.8** evaluates the energy separation between the O 1s edge (530.8 eV for the O 1s → π* transition of O_2 [S16] and 538.9 eV for the O1s → 3s transition of CO_2 [S15]) and the F 1s edge (688.3 eV for the F1s→ a_{1g} transition of SF_6(g) [S14]) at the two beamlines used in this work.

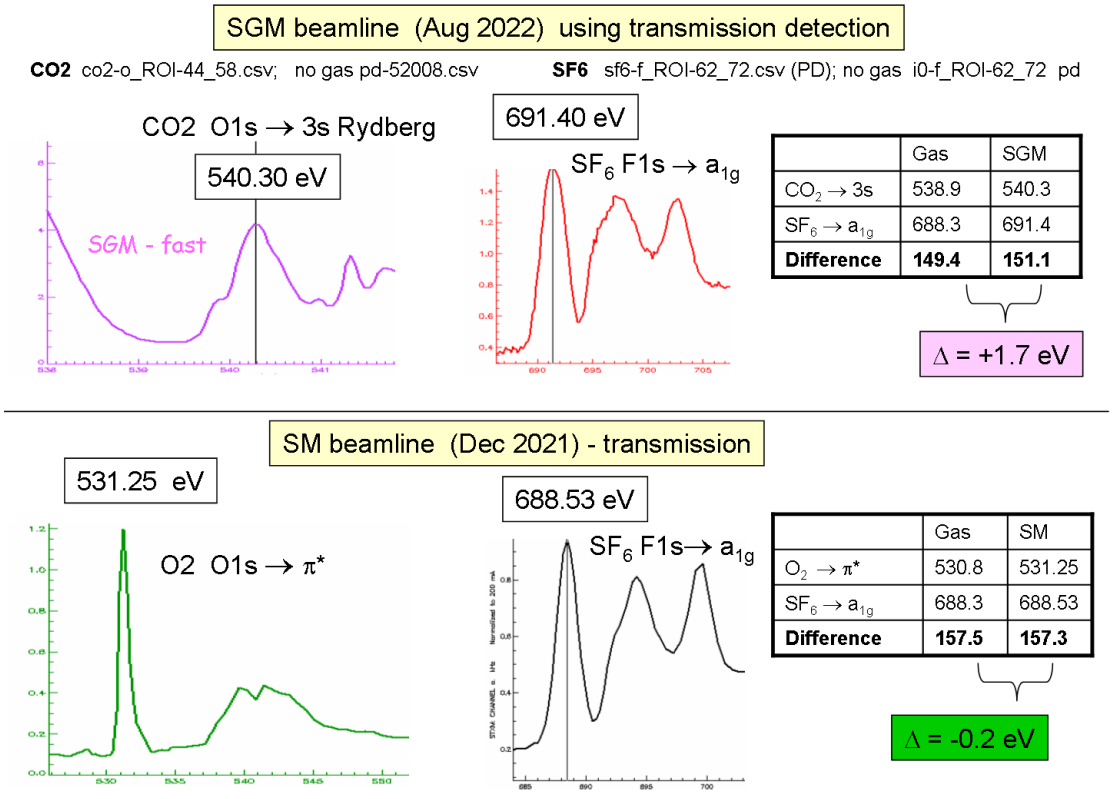

Figure S.8 Energy separation between the O 1s and F 1s edges measured at the CLS-SGM and CLS-SM beamlines using well-calibrated gas phase species (O_2 or CO_2 for O 1s, and SF_6 for F1s). The deviation from the true energy separation determined by gas phase inner shell electron energy loss spectroscopy is -0.2 eV at the CLS-SM beamline where the STXM measurements were performed, and +1.7 eV at the CLS-SGM beamline where TEY measurements were made.

SI.9 CLS-SM energy scale stability over a 5-day period

Figure S.9A and **S.9B** plots the observed positions of spectral features over a 5-day time period to illustrate the stability of the beamline energy scale. **Figure S.9C** presents Mn2p signals from MnO contamination on STXM zone plate (used to validate the stability of the Mn 2p energy scale).

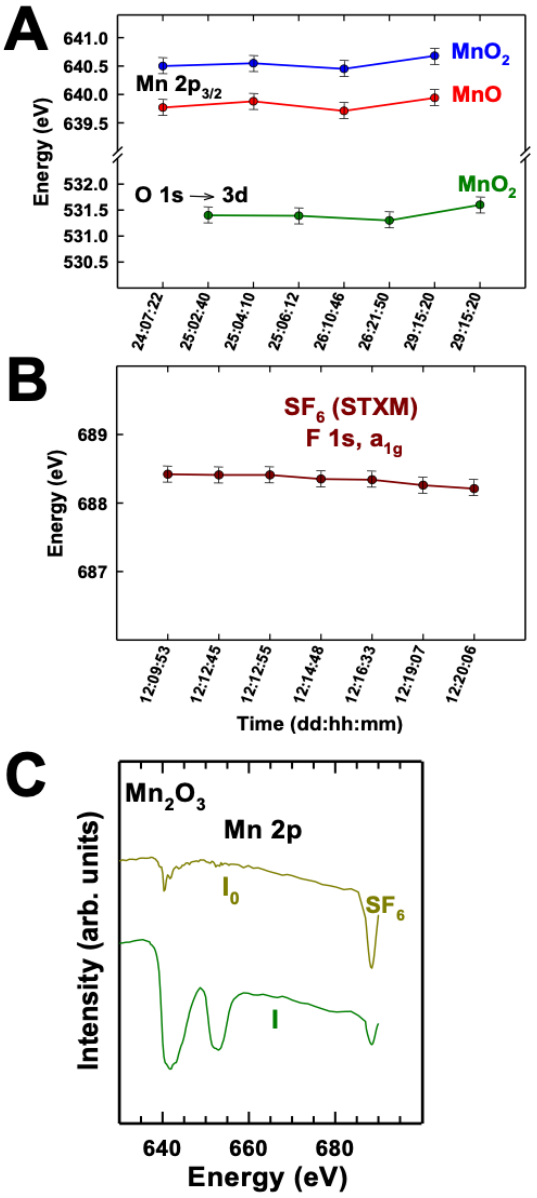

Figure S.9 plots the energies of specific features in **(A)** Mn 2p, O 1s and **(B)** F 1s regions observed over a 5 –day period at the CLS-SM STXM beamline. **(C)**. I and Io Mn 2p signals from stack measurement on Mn_2O_3 sample, the Io spectra shows the MnO contamination of the STXM zone plate used to validate the stability of the Mn 2p energy scale.

SI.10 Comparison of our results for MnO_2 to those of Gilbert [S4] and Toner [S17]

Figure S.10 compares the Mn 2p and O 1s spectra of β-MnO_2 measured by STXM (curve a) with those from the papers by Gilbert et al. [S4] (curve b) and by Toner et al. [S17] (curve c).

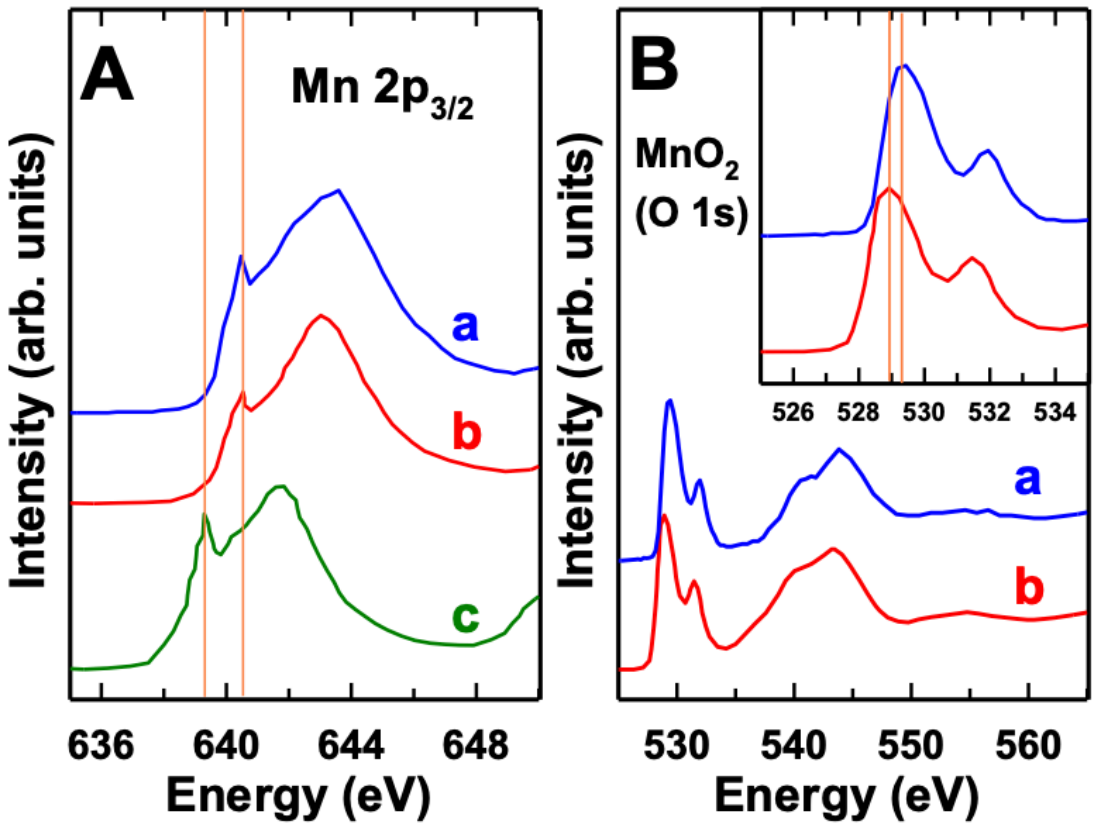

Figure S.10 Plot of **(A)** Mn 2p spectra and **(B)** O 1s spectra of β-MnO_2 measured with STXM (this work) to that of β-MnO_2 reported by Gilbert et al. [S4] and that of δ-MnO_2 reported by Toner et al. [S17]. (a) this work. (b) Gilbert et al [S4]. (c) Toner et al. [S17]. The vertical lines highlight the discrepancies in peak positions.

SI.11 O 1s spectra of compounds with different sulfur-oxygen bond lengths

Figure S.11 presents the O 1s absorption spectra of MnO and MnO_2 in comparison with compounds contain SO_4^- and SO_3^- group (H_2SO_4 and perfluorosulfonic acid, which is dominated by C-O-C ether groups, with minor contribution from terminal sulfonate groups) [S19] showing the effect of the SO_x groups (as ligand) on the O 1s spectral features.

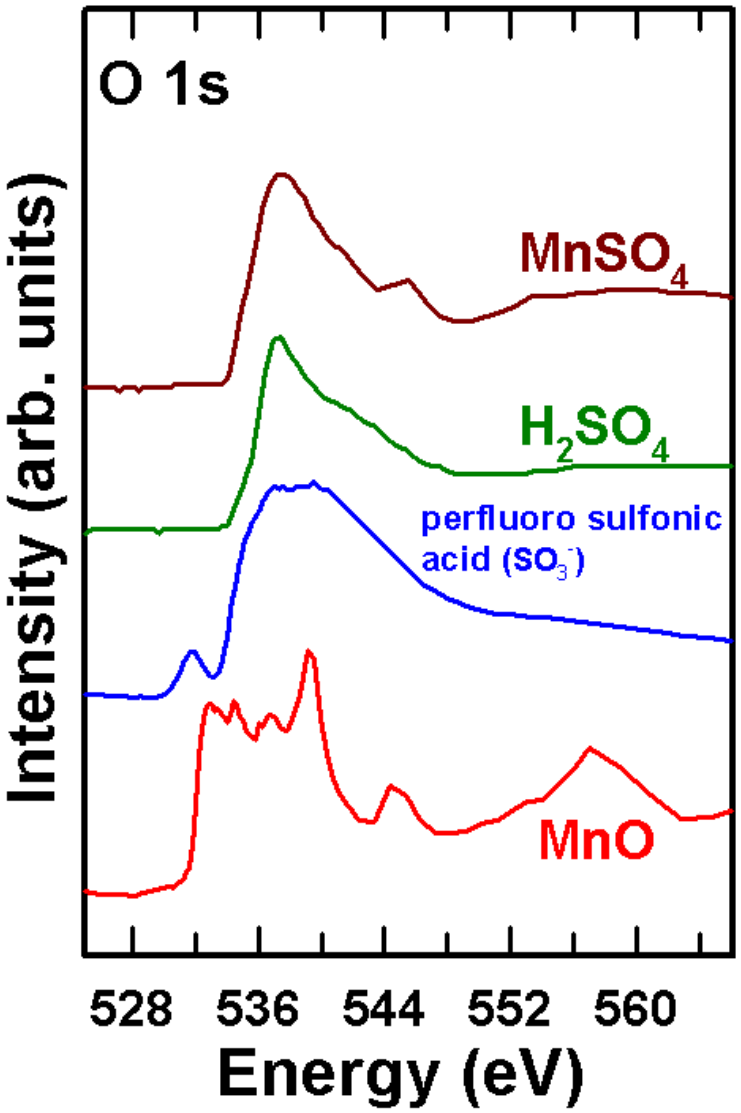

Figure S.11 O 1s absorption spectra of MnO and $MnSO_4$ (this work) in comparison with those of H_2SO_4 and perfluorosulfonic acid [S19]

SI.12 Comparison of the O 1s spectra of α-MnO_2 and β-MnO_2

Figure S.12A presents O 1s spectra of α-MnO_2 and β-MnO_2 measured by STXM. **Figure S.12B** presents expansion of O 1s → 3d "pre-edge" region (525 eV - 538 eV). α-MnO_2 and β-MnO_2 are very similar in terms of the O 1s → 3d spectral shape and peak positions. Thus, while these species can be differentiated at the Mn 2p edge (Fig. 3), they are indistinguishable at the O 1s edge.

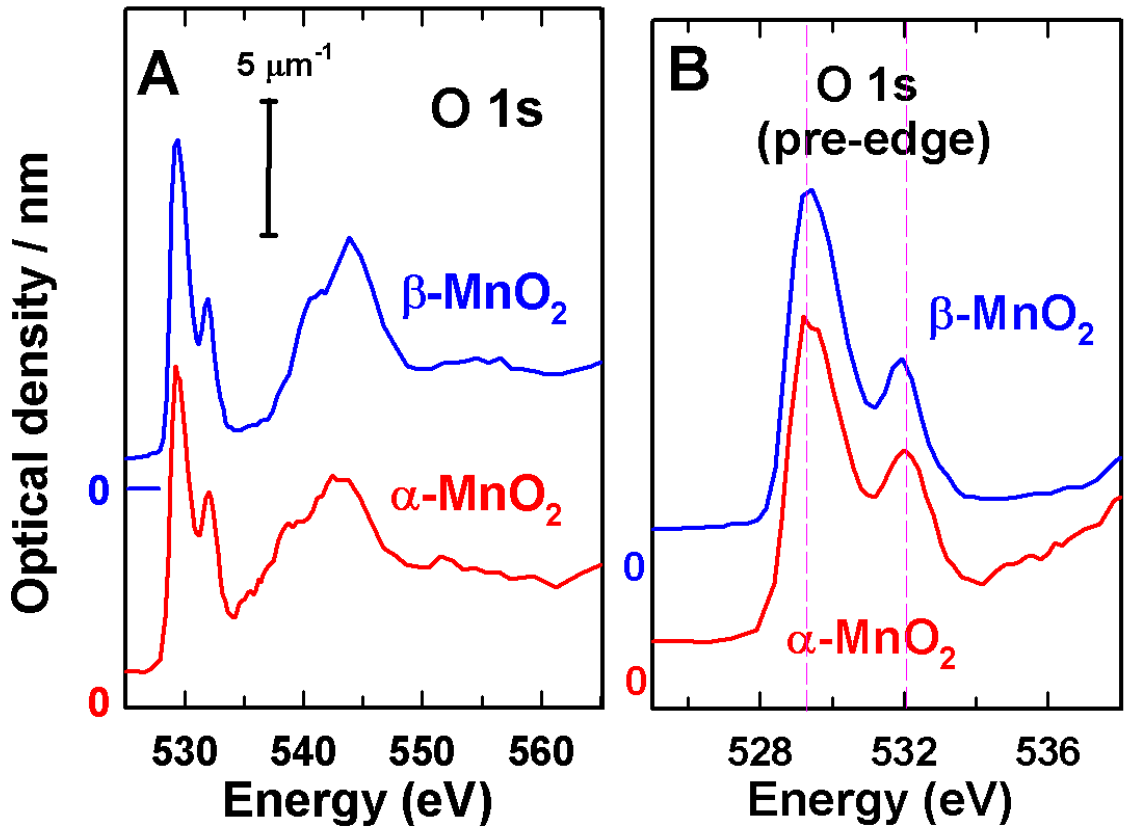

Figure S.12 **(A)** Comparison of the O 1s spectra of α-MnO_2 and β-MnO_2. **(B)** Expansion of O 1s → 3d features of α-MnO_2 and β-MnO_2.

SI.13 Comparison of analyses using Mn 2p, O 1s and (O 1s & Mn 2p) stacks

Figure S.13 presents color coded composites of MnO, Mn_2O_3 and MnO_2 maps of the 94-cycle discharged MnO_2.Zn ZIB sample, generated from 3 different analyses: Mn 2p only (**Fig. S.13A**), O 1s only (**Fig. S.13B**), and the combined O 1s and Mn 2p stacks (**Fig. S.13C**), after careful alignment and adjustment of pixilation. At first glance, it appears as if the three color composites show similar spatial distributions of the 3 MnOx species. However, closer inspection reveals that the O 1s maps differ significantly from the Mn 2p or combined (Mn 2p & O 1s) maps in that (i) the small regions of Mn_2O_3 distributed randomly in the area dominated by α-MnO_2 are missing, and (ii) the amounts of the MnO and Mn_2O_3 species are significantly overestimated (see the color coded thickness scales). On reflection, we realized that there was a fourth component in this system, namely Zn oxide. We have digitized the O 1s spectrum of ZnO nanorods reported by Jeon et al. [S20], converted it to an OD1 scale, and refit the O 1s stack using the four components whose O 1s OD1 spectra are plotted in **Fig. S.13D.** When this fourth component was also included in the fit the spatial distributions and quantitative amounts of the 3 MnOx species are closer to those determined from the Mn 2p (**Fig. S.13A**), and the combined (Mn2p & O1s) (**Fig. S.13C**) stacks. The map of the ZnO (**Fig. S.13F**) shows it is found all through the sample, but is most abundant in the region where MnO is found.

Combining & comparing the O 1s and Mn 2p results (a request by an astute reviewer), identified the anomalous result from analysis of the O 1s stack when analyzed using just the O 1s spectra of the MnOx species. This resulted in a much better understanding of the 94 charge/discharge cycled Zn/MnO_2 zinc ion battery sample, which we are now incorporating into a larger study of this system. In general, multi-edge spectromicroscopy studies of complex systems can provide (i) additional insights, (ii) potentially more reliable data (better statistics) and (iii) new information. O 1s measurements in the 528 – 533 eV range where O 1s → Mn 3d transitions occur can be particularly useful for *in-situ* studies of Mn oxide electrochemical transformations in batteries

and supercapacitors [S21] if the electrolyte layer (H_2O) is thick (>2 μm), since that can lead to absorption saturation at the Mn 2p edge, while the low energy part of the O 1s spectrum (526 – 533 eV), which is below the onset of O 1s absorption by water, is not affected by absorption saturation.

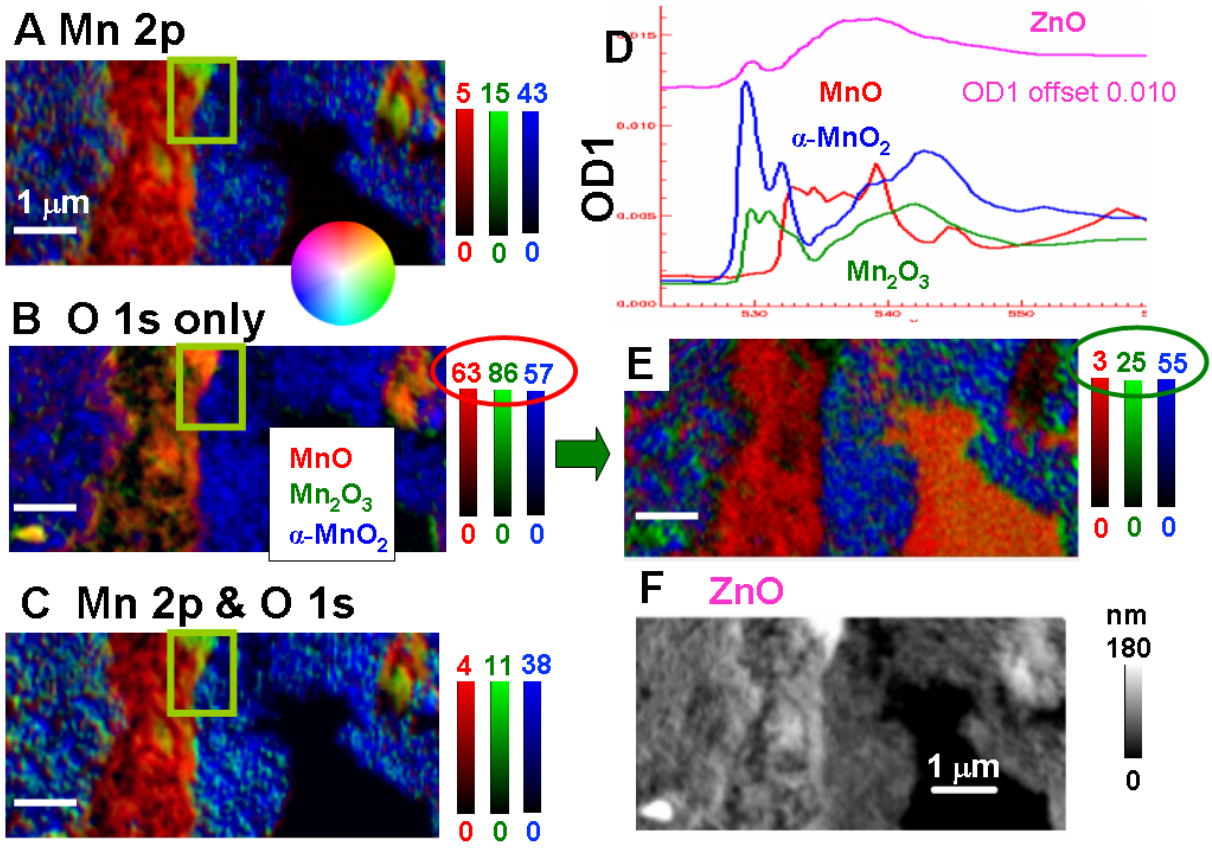

Figure S.13 Comparison of color coded composites of **(A)** MnO, **(B)** Mn_2O_3 and **(C)** α-MnO_2 maps of the 94-cycle discharged MnO_2.Zn ZIB sample, generated from 3 different analyses: Mn 2p only, O 1s only, and the combined O 1s and Mn 2p stacks, after careful alignment and adjustment of pixilation. (**D**) OD1 spectra of MnO, Mn_2O_3, α-MnO_2 and ZnO (digitized from [S20]). (**E**) Color composite of the 3 MnOx species, and (**F**) ZnO map from the 4-component stack fit.

SI.14 Example of linear combination fitting (LCF) of a mixed oxidation spectrum

Figure S.14 presents a linear combination fitting (LCF) analysis of the Mn $2p_{3/2}$ spectrum extracted from a specific region of the 94-cycle discharged MnO_2/Zn ZIB sample, for which the component maps are shown in **Fig. S.14A**. A region which has clear evidence of being a mixture

was identified by threshold masking the component maps for MnO (Fig. 5A) and Mn_2O_3 (Fig. 5B) and isolating pixels that were present in both of the derived maps. This selection is identified by the blue pixels in **Fig. S.14B**. The Mn $2p_{3/2}$ spectrum of those pixels was then extracted and fit to a linear combination of an adjustable constant (to fit non-Mn components such as Zn), and the Mn 2p reference spectra of MnO, Mn_2O_3 and MnO_2. **Figure S.14C** presents the results of that analysis, which indicates clearly the two dominant components (MnO and Mn_2O_3), plus a small amount of MnO_2. A significant advantage of this spectromicroscopy approach is that the color shading in the color coded composite mapping can be used to identify areas of interest in terms of spatial co-localization of species, which can then be verified using LCF analyses, as in this example.

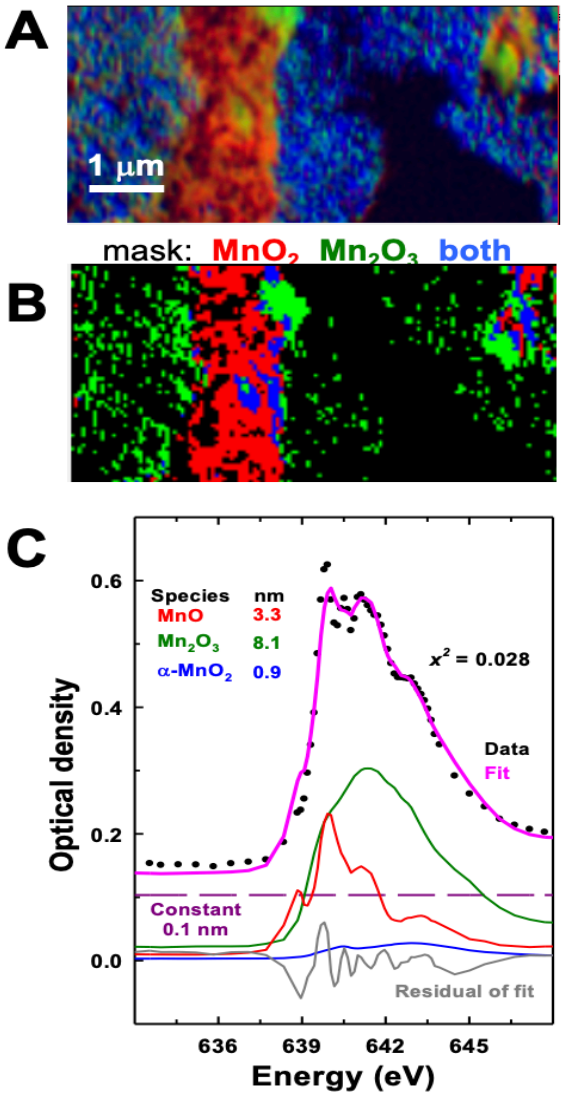

Figure S.14. **(A)** color coded composite of component maps derived from the stack fit of a Mn $2p_{3/2}$ stack a specific region of the 94-cycle discharged MnO_2/Zn ZIB sample. **(B)** Masks derived by histogram selection of regions which contain MnO (red), Mn_2O_3 (green), or simultaneously MnO and Mn_2O_3 (blue). (**C**) Linear combination fit (LCF) of the spectrum of the blue pixels. Since the reference spectra used in the fit are on an OD1 scale, the LCF coefficients are the averaged nm thickness of each of the three components in the blue pixels.

References

S1 G. Van der Laan, I. Kirkman, The 2p absorption spectra of 3d transition metal compounds in tetrahedral and octahedral symmetry, Journal of Physics: Condensed Matter 4 (1992) 4189.

S2 J.R. Bargar, G. Meigs, L. Cox, K.H. Nealson, Quantitative charge state analysis of manganese biominerals in aqueous suspension using Scanning Transmission X-ray, Geochimica et Cosmochimica Acta 67 (2003) 1089-1098.

S3 R. Qiao, T. Chin, S.J. Harris, S. Yan, W. Yang, Spectroscopic fingerprints of valence and spin states in manganese oxides and fluorides, Current Applied Physics 13 (2013) 544-548.

S4 B. Gilbert, B. Frazer, A. Belz, P. Conrad, K. Nealson, D. Haskel, J. Lang, G. Srajer, G. De Stasio, Multiple scattering calculations of bonding and X-ray absorption spectroscopy of manganese oxides, The Journal of Physical Chemistry A 107 (2003) 2839-2847.

S5 F. Bourdelle, E. Lloret, C. Durand, L. Airaghi, Evaluation of scanning transmission X-ray microscopy at the Mn L2, 3-edges as a potential probe for manganese redox state in natural silicates, Physics and Chemistry of Minerals 48 (2021) 18.

S6 M.C. Biesinger, B.P. Payne, A.P. Grosvenor, L.W. Lau, A.R. Gerson, R.S.C. Smart, Resolving surface chemical states in XPS analysis of first row transition metals, oxides and hydroxides: Cr, Mn, Fe, Co and Ni, Applied Surface Science 257 (2011) 2717-2730.

S7 R. Burns, Outline of crystal field theory, Cambridge Topics in Mineral Physics and Chemistry. Cambridge University Press (1993) 7.

S8 L. Garvie, A. Craven, High-resolution parallel electron energy-loss spectroscopy of Mn L2, 3-edges in inorganic manganese compounds, Physics and Chemistry of Minerals 21 (1994) 191-206.

S9 D.M. Sherman, The electronic structures of manganese oxide minerals, American Mineralogist 69 (1984) 788-799.

S10 F.M. de Groot, J. Fuggle, B. Thole, G. Sawatzky, 2p x-ray absorption of 3d transition-metal compounds: An atomic multiplet description including the crystal field, Physical Review B 42 (1990) 5459.

S11 Schmalz, Michael, Robert Schöllhorn, and Robert Schlögl, d−Electron Density in Formal d^0 Systems from Multiplet Splitting in the Photoelectron Spectrum of Permanganates, Angewandte Chemie International Edition in English 30.8 (1991) 967-969.

S12 B.L. Henke, E.M. Gullikson, J.C. Davis, X-ray interactions: photoabsorption, scattering, transmission, and reflection at E= 50-30,000 eV, Z= 1-92, Atomic Data and Nuclear Data tables 54 (1993) 181-342.

S13 Patnaik, P., *Handbook of inorganic chemicals* 529 (2003) McGraw-Hill New York.

S14 R.N. Sodhi, C. Brion, Reference energies for inner shell electron energy-loss spectroscopy, Journal of electron spectroscopy and related phenomena 34 (1984) 363-372.

S15 Prince, K.; Avaldi, L.; Coreno, M.; Camilloni, R.; De Simone, M.Vibrational structure of core to Rydberg state excitations of carbon dioxide and dinitrogen oxide. J. Phys. B: At., Mol. Opt. Phys. 32 (1999 2551-2567.

S.16 Y. Ma, C. T. Chen, G. Meigs, K. Randall, and F. Sette , High-resolution *K*-shell photoabsorption measurements of simple molecules, Phys. Rev. A 44 (1991) 1848

S.17 B. Toner, S. Fakra, M. Villalobos, T. Warwick, G. Sposito, Spatially resolved characterization of biogenic manganese oxide production within a bacterial biofilm, Applied and environmental microbiology 71 (2005) 1300-1310.

S.19 R. Hayes, B.Sc. thesis McMaster University, 2014 (unpublished)

S.20 E.H. Jeon, S.Yang, Y. Kim, N. Kim , H.-J. Shin, J. Baik, H.S. Kim and H.Lee, Comparative study of photocatalytic activities of hydrothermally grown ZnO nanorods on Si(001) wafer and FTO glass substrates, Nanoscale Research Letters (2015) 10:361

S.21 H. Eraky (2024). Ex-situ and In-situ Soft X-Ray Spectro-Microscopy Studies of Manganese Oxide Electrodes for Energy Storage Applications. PhD Thesis, McMaster University.